Journal of Energy Storage 73 (2023) 109131

Contents lists available at ScienceDirect

Journal of Energy Storage

journal homepage: www.elsevier.com/locate/est

Research papers

Design and development of NbTiVZr porous high entropy alloys for energy applications

Ayesha Siddique [a], Talha Abid [a], M. Aftab Akram [a], Talha Bin Yaqub [b], M. Ramzan Abdul Karim [c], Filipe Fernandes [b,d], Rizwan Khan [e], Khurram Yaqoob [a,*]

[a] School of Chemical and Materials Engineering (SCME), National University of Sciences and Technology (NUST), H-12 Islamabad, Pakistan
[b] University of Coimbra, CEMMPRE - Centre for Mechanical Engineering Materials and Processes, Department of Mechanical Engineering, Rua Lu's Reis Santos, 3030-788 Coimbra, Portugal
[c] Department of Materials Science and Engineering, Ghulam Ishaq Khan Institute of Engineering Sciences and Technology, Topi, Swabi 23640, KPK, Pakistan
[d] ISEP School of Engineering, Polytechnic of Porto, Rua Dr. António Bernardino de Almeida 431, 4200072 Porto, Portugal.
[e] Department of Bio Nanotechnology, Hanyang University, South Korea

ARTICLE INFO

Keywords:
Electrode material
Refractory high entropy alloys
Selective dissolution
Porous high entropy alloys
Metallic foams
Supercapacitors

ABSTRACT

Porous NbTiVZr refractory high entropy alloys have been developed by a novel method that is based on the addition of yttrium to the base high entropy alloy and its subsequent removal by electrochemical dealloying process. Microstructure and crystal structure characterization of as-cast alloys confirmed the segregation of yttrium at interdendritic regions. Successful removal of yttrium from interdendritic region has been confirmed by microstructure and crystal structure characterization of dealloyed samples. NbTiVZr foams with varying levels of porosity were successfully developed and characterized. Electrochemical performance of the developed foams was investigated by cyclic voltammetry (CV), galvanostatic charge discharge (GCD), and electrochemical impedance spectroscopy (EIS). High areal capacitance of 82.66 mF cm^{-2} at scan rate of 2 mV s^{-1} was exhibited by one of the developed electrodes. The electrode displayed capacitance retention of 104 % after 5000 cycles at current density of 1 mA cm^{-2}. The excellent electrochemical performance demonstrated by the NbTiVZr refractory high entropy foams highlights their potential as suitable candidates for supercapacitor electrode.

1. Introduction

The need to develop renewable, reliable and environmental friendly sources of energy is increasing due to energy sustainability and environmental concerns [1,2]. Supercapacitors have gained substantial attention as alternate to conservative energy storage devices owing to their fast charge-discharge, longer stability, moderate energy density, [3] high-power density, long life cycle, fast power energy delivery [4] low weight, wide temperature range (−40 °C to 70 °C), flexible packaging and low maintenance [5]. However, low capacitance, low energy density, high self-discharge, and low voltage per cell limits their practical use. Development of new electrode materials for supercapacitors can help in this regard [6]. Carbon materials, conducting polymers, transition metal oxides and hydroxides have become promising materials for supercapacitor electrodes [7–13]. Transition metal oxides (TMOs) are an attractive candidate for supercapacitor applications because of their multiple oxidation states [14]. Selection of appropriate electrode material is important as it influences the performance of supercapacitors [5]. Development of electrode materials with outstanding electrochemical performance, despite the advancements in supercapacitor technology, is still a challenge.

High entropy alloys (HEA) are the new class of alloys that generally consist of 5 to 8 principal alloying elements and are known to preferably form one or more solid solution phases [4]. HEAs have shown an excellent combination of mechanical properties and are being considered as alternatives to conventional materials for structural applications [15–17]. The potential of high entropy alloy for energy storage and catalysis applications has been explored in some of the recent studies [18–27]. The electrochemical performance of high entropy alloys can be further enhanced by increasing the specific surface area through the insertion of porosity. Porous electrode materials with relatively large specific surface areas can increase the surface area, shorten the path for transportation of ions/electrons, and also increases the accessibility of electrolyte ions to internal active sites thereby increasing the

* Corresponding author.
E-mail address: khurram.yaqoob@scme.nust.edu.pk (K. Yaqoob).

https://doi.org/10.1016/j.est.2023.109131
Received 18 June 2023; Received in revised form 10 September 2023; Accepted 27 September 2023
Available online 7 October 2023

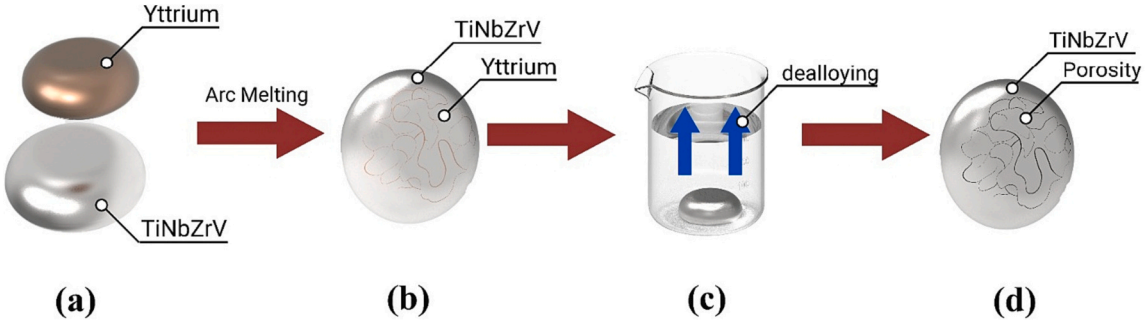

Fig. 1. Schematic diagram of process of development of high entropy foams.

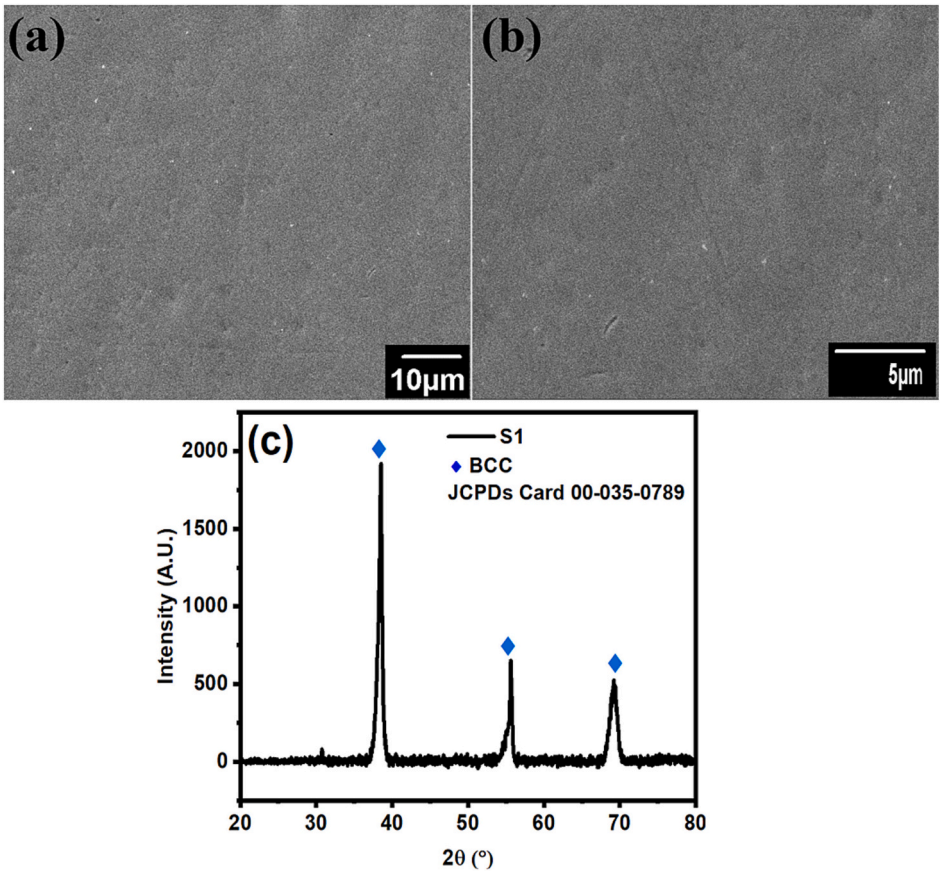

Fig. 2. (a,b) SEM images and (c) XRD pattern of the base NbTiVZr HEA (S1).

Table 1
The values of ΔH{A,B} for atomic pairs of the selected high entropy alloy system.

	Nb	Ti	V	Zr	Y
Nb	–	2	−1	4	30
Ti		–	−2	−0.2	15
V			–	−4	17
Zr				–	9
Y					–

capacitance value [28,29]. Method used for the insertion of porosity can greatly affect the microstructure and affect its electrochemical performance [1].

A variety of synthesizing routes have been reported in literature for developing porous electrode materials. Soft templating method is used to prepare various types of metal oxides and porous phosphates material with different morphologies and compositions. However porous structure and crystallinity of electrode materials are affected at higher temperatures [30]. Nano casting is the versatile method for the synthesis of highly crystalline and more ordered porous structures [31]. Silica templates used in this method should be removed completely as they are electronically insulating [32]. Colloidal crystal templating (CCT) method is used to obtain well-ordered, interconnected pores of large sizes. However large shrinkage is observed with polymeric templates and pore size will be smaller than the predicted due to shrinkage of porous structure [33]. Sol-gel method is used to synthesize aerogels through superficial drying or solvent exchange methods [34]. However, sintering step during thermal treatment can result in densification of material and reduce the pore volumes and surface areas [35]. Wood templating combined with sol-gel processes enables the development of open and interconnected pores that are beneficial for mass transport and

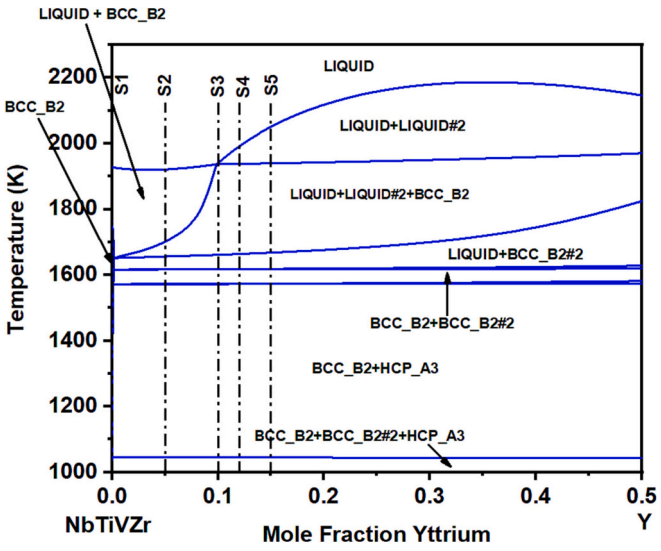

Fig. 3. Pseudo-binary phase diagram of NbTiVZr-Y HEA system.

facilitate the diffusion of ions. Pyrolyzable performers are used as sacrificial templates to obtain different size and shapes of pores [36]. However, the pyrolysis at high temperature can decrease the porosity resulting in accumulation of gases. Also, the interconnected pores are tortuous and randomly distributed limiting the mass transfer in porous electrode [37]. Ice templating, also called freeze casting is the versatile method for producing 3D porous network but it is susceptible to solvent contamination [38].

Refractory metals exhibit high melting points, high strength, corrosion resistance, high temperature softening resistance, and provide low resistance to electron flow because of their high electrical conductivity [39]. Refractory metals based porous high entropy alloys can therefore be a good candidate for supercapacitor applications because of their high electrical conductivity, high surface area, and better mechanical properties. The present study is focused on insertion of different levels of porosity in NbTiVZr high entropy alloy by a novel method proposed during the present study and on investigating the electrochemical performance of developed foams as an electrode material for supercapacitor applications.

2. Experimental procedure

High purity niobium, titanium, vanadium, zirconium, and yttrium (purity $>$ 99.95 %) metals were used as raw materials for the development of high entropy foams. Development of high entropy alloys was carried out in two stages. In the first stage, the constituents of NbTiVZr high entropy alloy were placed in water cooled copper hearth and chamber of the furnace was initially evacuated to 3×10^{-5} mbar followed by insertion of high purity argon to facilitate melting under controlled atmosphere. Titanium has strong affinity toward oxygen. Melting of pure titanium was carried out, prior to the melting of NbTiVZr HEA, to remove any traces of oxygen left in the chamber. Each NbTiVZr HEA sample was melted for around 40–45 s and remelted after turning it upside down. The process was repeated for five time to ensure chemical homogeneity. In the second stage, varying amount of yttrium (5, 10, 12 and 15 wt%) was added to the developed NbTiVZr high entropy alloy button by following the same procedure as was used for the development of NbTiVZr HEA. Weight loss of the samples was recorded and was found to be $<$0.5 % after melting. Dealloying was carried out for removal of yttrium from interdendritic areas, for the development of high entropy foams. Samples for electrochemical dealloying were immersed in 5 % aqueous solution of nitric acid for 24 h. Samples after electrochemical dealloying were thoroughly cleaned by ultrasonication in water and in ethanol, dried, and subjected to different characterization. Schematic illustration of development of high entropy foams is shown in the Fig. 1.

Standard metallographic procedures were used for preparation of samples for microstructural investigation which was carried out by using scanning electron microscope (SEM; JEOL JSM-6490LA). Crystal structure characterization of the developed high entropy alloy and their respective foams was carried out by performing X-ray diffraction measurements on a Bruker D2 phaser (equipped with Cu Kα radiation).

Electrochemical characterization of developed foam was conducted in a three-electrode cell configuration by using a potentiostat (21,084 Interface 1010E, USA). Cyclic voltammetry and galvanostatic charge discharge tests were carried out in 1 M Na_2SO_4 solution with HEA electrode, platinum (Pt) wire, and Ag/AgCl serving as working electrode, counter electrode, and reference electrode respectively. The exposed surface area of HEA working electrodes for all electrochemical measurements was around 7 × 7 mm. Areal capacitance from the GCD curves was calculated by using Eq. (1).

$$AC = \frac{I}{S} \times \frac{t}{\Delta V} \tag{1}$$

where, I is the current (mA), t is the discharging time (s), S is the exposed geometric area, and ΔV is the discharging voltage (V). Electrochemical impedance spectroscopy (EIS) measurements were performed at 10 mV amplitude in frequency range of 100 kHz–10 MHz to understand the kinetic properties.

3. Results and discussions

3.1. Characterization techniques

The present study is aimed at the development of a method for the development of NbTiVZr foams and explore their potential for supercapacitor applications. SEM and XRD results of the base NbTiVZr HEA (named as S1) are shown in the Fig. 2.

SEM images of the sample S1 (Fig. 2a, b) pointed out the presence of a single phase in the developed alloys which was identified as bcc with the help of XRD analysis (Fig. 2c). The method proposed during the present study has been adopted from the method proposed for the development of refractory metals based HEA [40]. It is based on the addition of such a filler metal to base HEA system that is completely or partially insoluble in the base HEA and tends to segregate to the interdendritic areas during solidification. As interdendritic area are interconnected, subsequent removal of the filler metal from interdendritic areas can help in development of interconnected porosity. The enthalpy of mixing of filler element with the constituent of the base HEA should be positive enough to cause its segregation to the interdendritic areas but should not be so positive that it may cause liquid phase separation. Selection of filler element is of paramount significance. Yttrium was selected as filler element for the development of NbTiVZr foams because of its moderately positive enthalpy of mixing with the constituent of the selected HEA system and its density. Enthalpies of mixing data of binary combinations of the constituent of the selected HEA and filler elements is listed in Table 1.

As shown in the Table 1, yttrium possessed positive enthalpy of mixing with constituent of the selected HEA system and is therefore expected to segregate to the interdendritic region during solidification. To verify the aforementioned hypothesis, pseudo-binary phase diagram of NbTiVZr-Y was calculated with the help of Thermocalc software using TCHEA database. The calculated NbTiVZr-Y pseudo binary phase diagram is shown in Fig. 3.

High entropy alloys with varying amounts of yttrium (5 at.%, 10 at. %, 12 at.%, and 15 at.%) were shortlisted for the present study to evaluate the effect of addition of yttrium on the microstructure of the base HEA and possibility of development of high entropy foams with

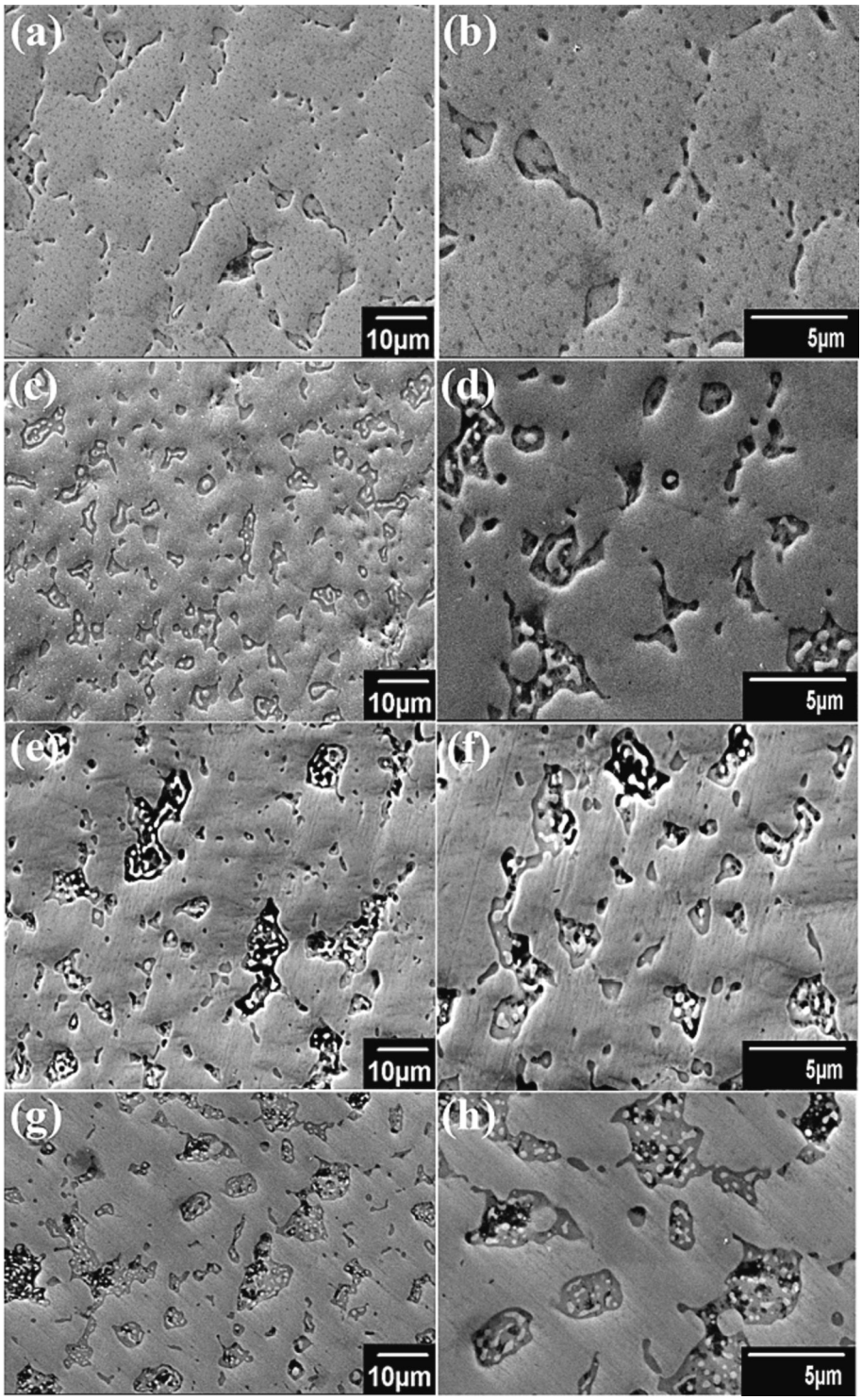

Fig. 4. SEM images of (a, b) as-cast S2 (c, d) as-cast S3 (e, f) as-cast S4 and (g, h) as-cast S5.

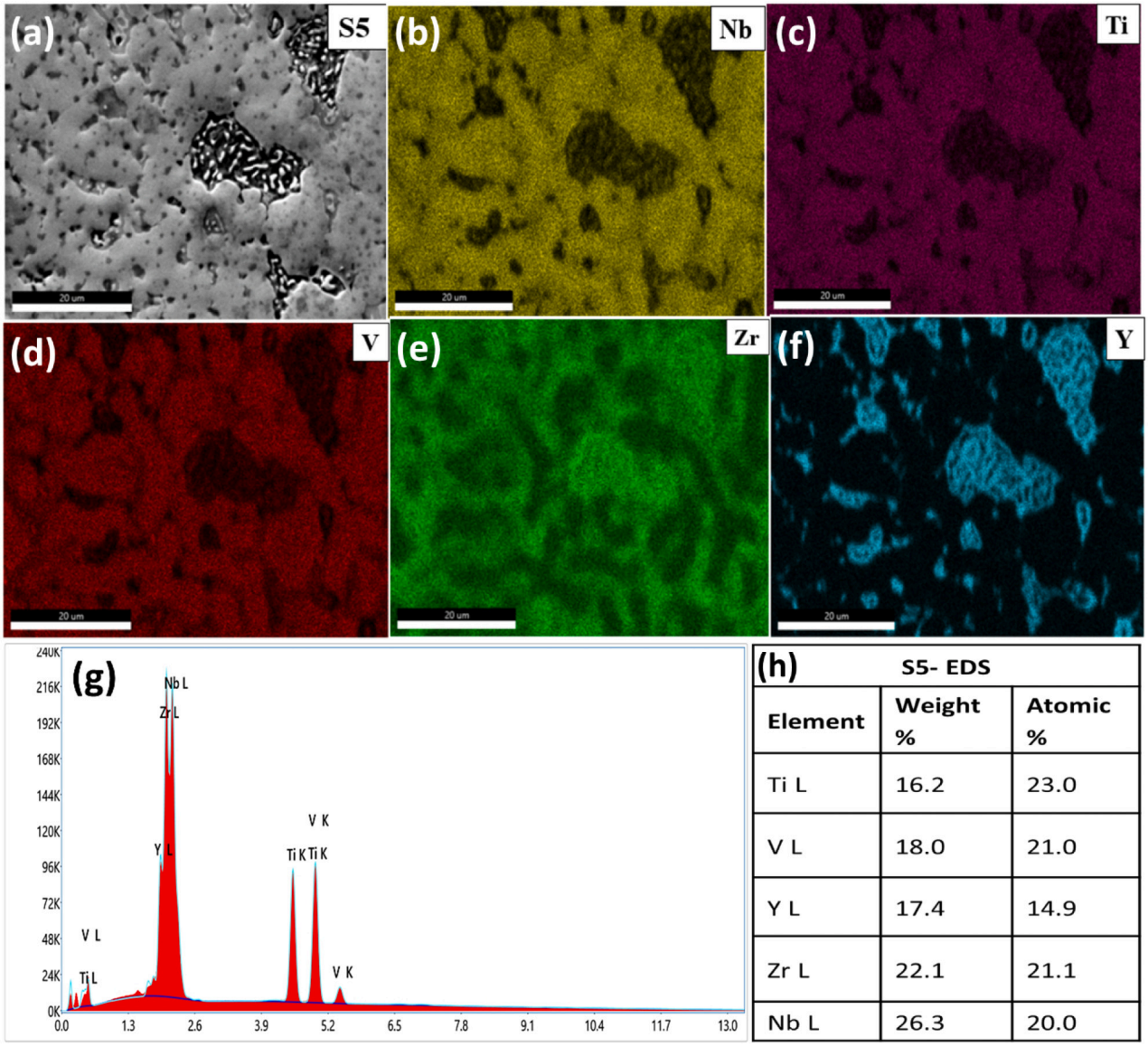

(h) S5- EDS

Element	Weight %	Atomic %
Ti L	16.2	23.0
V L	18.0	21.0
Y L	17.4	14.9
Zr L	22.1	21.1
Nb L	26.3	20.0

Fig. 5. (a–f) EDS mapping of as-cast S5 (g) EDS spectrum of as-cast S5 sample and (h) percentages of elements in the as-cast S5.

varying levels of porosities. As-cast NbTiVZr samples containing 5 at.% Y, 10 at.% Y, 12 at.% Y, and 15 at.% Y were named as S2, S3, S4 and S5 respectively. Microstructural analysis of the developed as-cast samples was carried out with the help of scanning electron microscope. SEM images of the as-cast samples are shown in the Fig. 4.

SEM images of as-cast high entropy alloys (S2-S5) showed presence of a matrix phase and interdendritic areas. The percentage of interdendritic areas was found to increase as the amount of yttrium added in the NbTiVZr HEA increased. To study elemental distribution in the matrix and in the interdendritic areas, EDS mapping was carried out. Results of EDS mapping of the S5 sample are shown in the Fig. 5 as an example.

As shown in the Fig. 5, niobium, titanium, and vanadium were found to be uniformly distributed throughout the matrix phase whereas presence of zirconium was evidenced both in the matrix as well as in the interdendritic regions. The EDX analysis confirmed segregation of yttrium to the interdendritic areas.

In order to remove yttrium from interdendritic areas for the development of porosity, samples were immersed in nitric acid solution for 24 h for electrochemical dealloying process. Microstructural and crystal structure characterization of the de-alloyed sample was carried out with the help of SEM, EDS, and XRD analysis. Foams of S2, S3, S4 and S5 compositions, obtained after electrochemical dealloying, were named as FS2, FS3, FS4 and FS5 respectively. SEM images of the dealloyed samples (FS2–FS5) are shown in Fig. 6.

SEM images of the dealloyed samples confirmed removal of yttrium from interdendritic areas resulting in the development of high entropy foams. To study the elemental distribution in the dealloyed samples, EDS mapping was carried out. The results of EDS mapping are shown in Fig. 7.

As shown in the Fig. 7(f), EDS mapping confirmed dissolution of yttrium from the interdendritic areas for the development of high entropy foams. XRD analysis of the developed high entropy alloys before and after the electrochemical dealloying is shown in Fig. 8.

XRD patterns of the as-cast samples showed presence of the peaks corresponding to the presence of bcc phase, and hcp phase. By combining the SEM and XRD results, it was concluded that the BCC phase corresponded to the matrix phase whereas HCP phase corresponded to the yttrium present in the interdendritic areas. Relative intensities of the peaks corresponding to HCP phase were found to increase with increase in the amount of added yttrium in the sample. XRD patterns of dealloyed samples (FS2-FS5) only showed presence of peaks

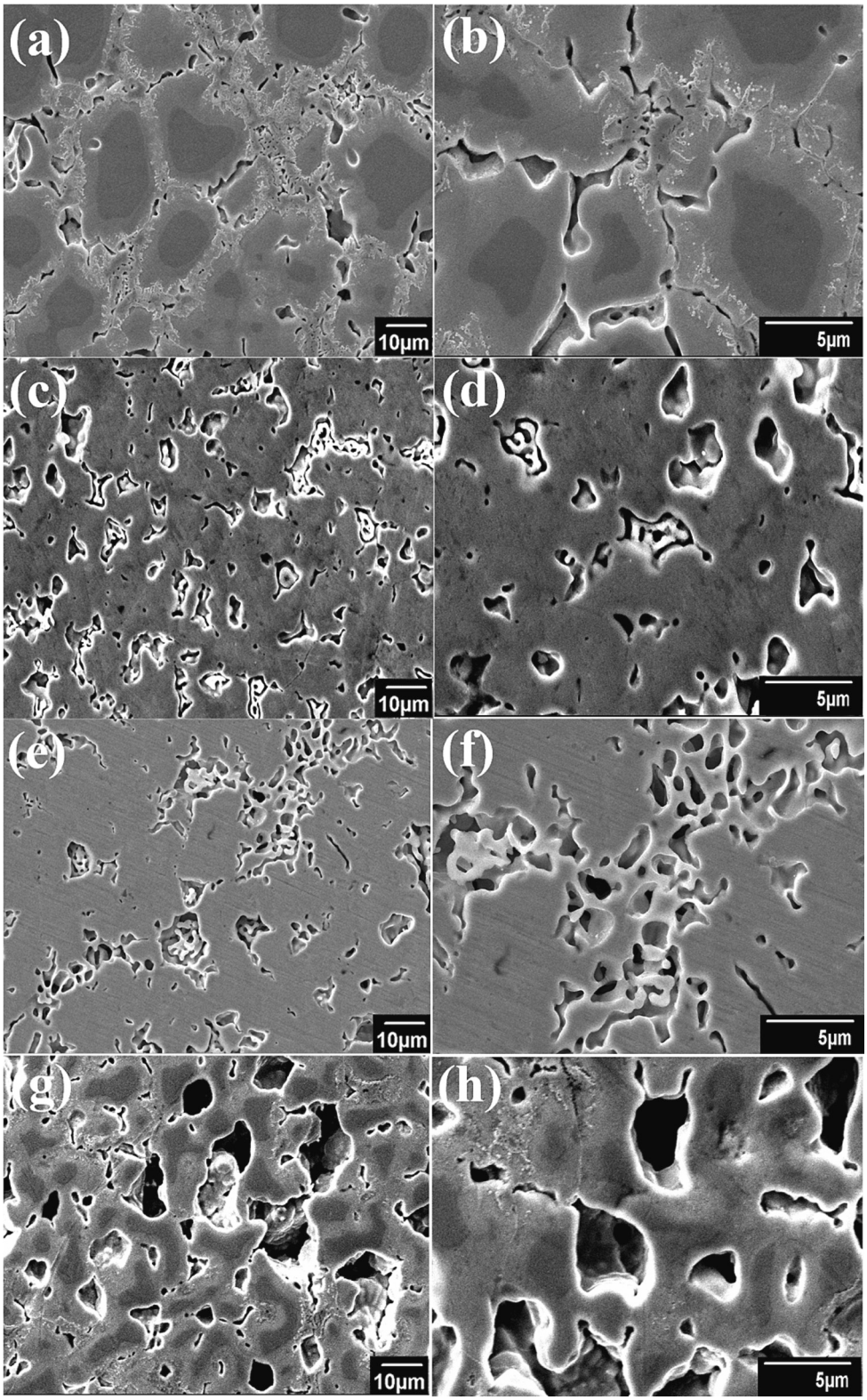

Fig. 6. SEM images of (a, b) FS2 (c, d) FS3 (e, f) FS4 and (g, h) FS5.

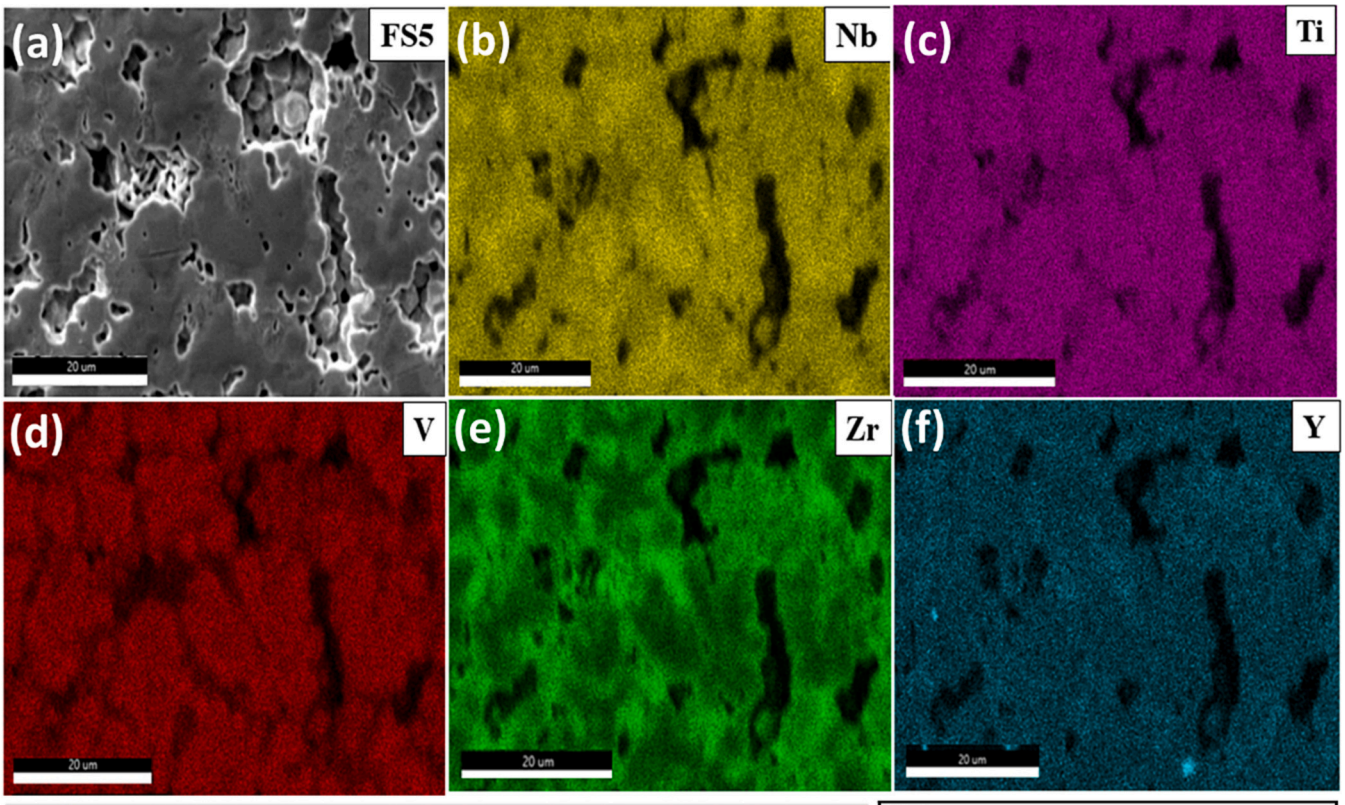

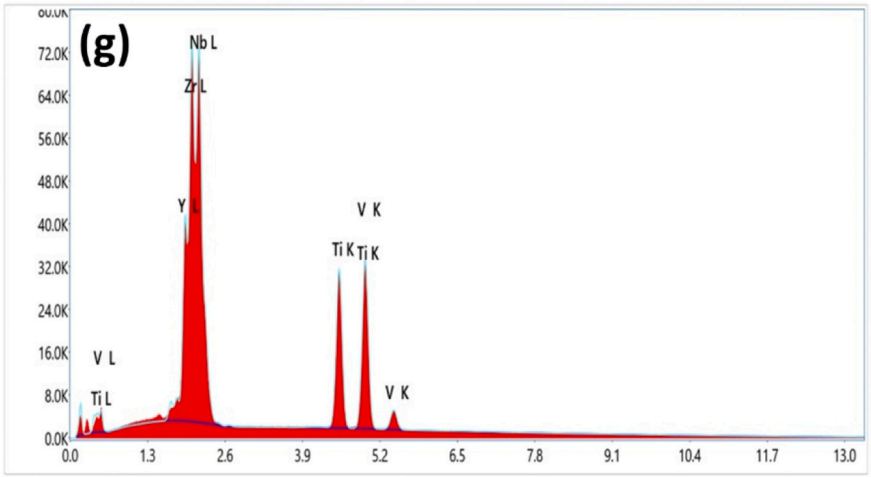

(h) FS5- EDS

Element	Weight %	Atomic %
Ti K	18.5	26.6
V K	17.7	24.8
Y L	6.2	5.5
Zr L	28.2	21.3
Nb L	29.4	21.8

Fig. 7. (a-f) EDS mapping of FS5, (g) EDS spectrum of FS5 sample and (h) Percentages of the elements in FS5.

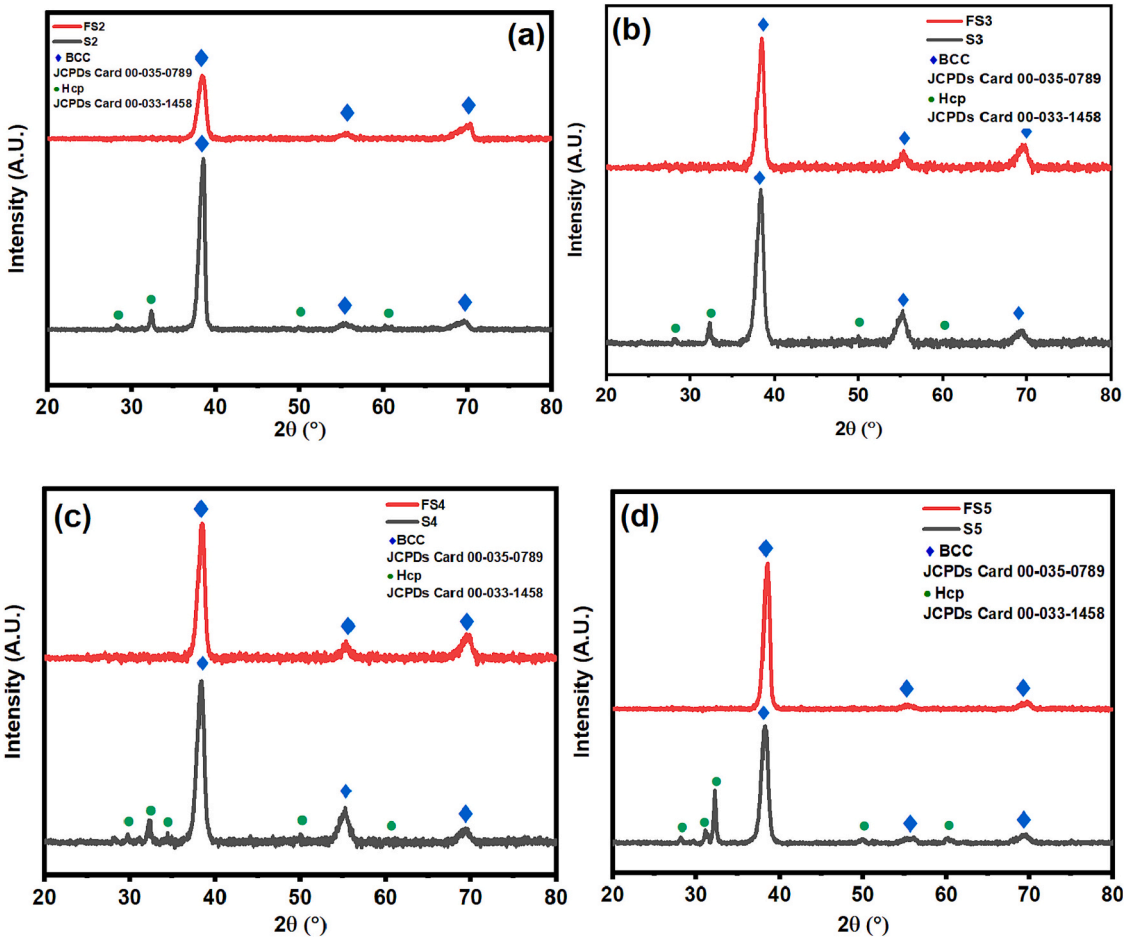

Fig. 8. XRD patterns of (a) S2 & FS2 (b) S3 & FS3 (c) S4 & FS4 and (d) S5 & FS5.

corresponding to the presence of BCC phase. Presence of peaks corresponding to hcp phase was not evidenced in any of dealloyed samples; thereby confirming removal of yttrium from interdendritic regions. SEM, EDS and XRD analysis confirmed the successful removal of yttrium from interdendritic areas and development of NbTiVZr high entropy foams.

3.2. Electrochemical testing

Electrochemical testing of the developed electrodes was carried out to study the effect of insertion of porosity in NbTiVZr HEA on its electrochemical properties. The first step in this regard was selection of a suitable electrolyte for electrochemical testing of developed samples. Acidic (H_2SO_4), and alkaline (KOH) electrolytes exhibit higher ionic conductivity [41] but are highly corrosive which may lead to peeling off the electrode material from substrate. Neutral electrolytes (e.g., Li_2SO_4, Na_2SO_4) [42] show lower ionic conductivities, but they exhibit large working potential windows, and are less corrosive [43]. The maximum operating potential window in aqueous electrolytes (H_2SO_4, KOH, Na_2SO_4, Li_2SO_4) is determined by water decomposition limit (~1.23 V, evolution of H_2/O_2 at 1 atm pressure, at room temperature). However, there are reports showing the possibility to go beyond the limit using different configurations and certain type of aqueous electrolyte [43,44].

The foam sample FS5 was used as the test sample and its electrochemical testing was performed in 1 M aqueous solution of KOH, H_2SO_4, and Na_2SO_4 respectively. Cyclic voltammetry of FS5 was performed in 1 M KOH in various potential windows (Fig. 9(a)). However, sample was only stable in negative (anodic) region i.e. −1 to 0 V (ΔV = 1 V). Gas evolution started at counter (platinum) electrode above 0 V making it impossible to test it in the positive voltage range. The sample FS5 was also tested in 1 M H_2SO_4 electrolyte (Fig. 9(b)). It showed some stability in −0.5 to 0.5 V potential window with a small area under the curves. Sharp rise in reduction and oxidation currents was observed before −0.5 V and after 0.5 V. These findings indicated the inability of sample to perform in wide potential range in case of alkaline and acidic electrolytes. Testing of the sample was also performed in 1 M Na_2SO_4 aqueous solution in various potential ranges of −1–+1 V (ΔV = 2 V), 0.7–0.7 V (ΔV = 1.4 V), −0.5–0.5 V (ΔV = 1 V), −1–0 V (ΔV = 1 V), 0–1 V (ΔV = 1 V), −0.6–0.2 V (ΔV = 0.8 V), and −0.2–0.6 V (ΔV = 0.8 V) respectively [CV graph in Fig. 9(c)]. Current response in case of −1 V to +1 V (ΔV = 2 V) was found to be higher as compared to rest of potential ranges. In this region not only the area under the curve was significant but also oxidation (0.25 V) and reduction peaks (0.0 V) were found to be more significant in case of −1 to +1 V. This suggested that intercalation/deintercalation processes or reversible redox reactions were more favourable in higher potential window, while low current response in small potential windows could derive from double layer contribution. With neutral electrolyte i.e. Na_2SO_4, extended potential window can be stabilized [42]. The reasons for getting extended potential window are the following: (a) Na_2SO_4 neutral aqueous electrolyte results in an equilibrium between H^+ and OH^- ions which restricts the availability of OH^- anions and H^+ (i.e., H_3O^+) to the electrodes for O_2 and H_2 evolution. (b) The electrolyte decomposition potential is higher than the thermodynamic decomposition of water (1.23 V) because of strongly solvated cations and sulphate anions [45]. Therefore, 1 M Na_2SO_4 was chosen as an electrolyte and electrochemical measurements of all the sample (S1-FS5) were performed in three-electrode setup with extended potential window of −1–+1 V (ΔV = 2 V).

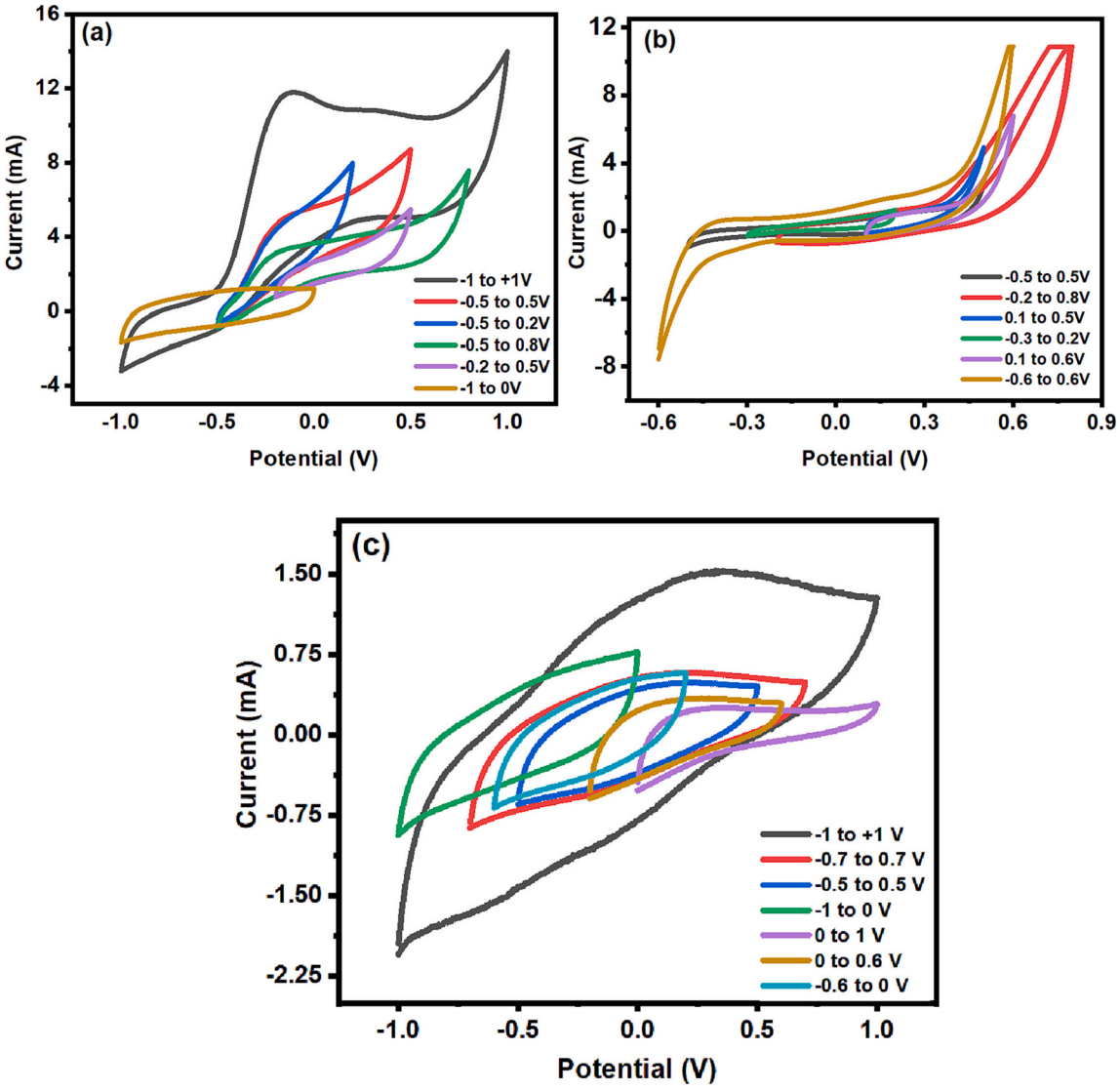

Fig. 9. CV analysis of FS5 in 1 M aqueous solution of (a) KOH, (b) H_2SO_4, and (c) Na_2SO_4, in different potential windows.

3.2.1. *Cyclic voltammetry analysis*

Electrochemical testing of developed HEA (S1) and foams (FS2-FS5) was carried out in 1 M Na_2SO_4 by using Ag/AgCl and platinum wire as reference and counter electrodes respectively. Cyclic voltammetry was performed in the potential window of −1 V–+1 V at the scan rates ranging from 10 mVs^{-1}–100 mVs^{-1}. Results of cyclic voltammetry are shown in Fig. 10.

All the samples showed quasi-rectangular features with oxidation peak at 0.25 V and reduction peak at 0.0 V which indicated that all the samples undergo successive redox reactions in the entire potential window. This could be attributed to the cumulative effect from adsorption of charges on sample surface and intercalation/deintercalation of cations (H^+ and Na^+) throughout the active porous structure [1]. The absence of clear redox peaks and quasi-rectangular features confirmed that charge storage was either because of the cation's fast adsorption/desorption process on the surface or due to intercalation/deintercalation process. The areal capacitance (Ca) of the samples were calculated from the CV curves using the following equation [46] and are presented in Fig. 10.

$$Ca = \frac{I\,(V)dV}{Av\,(V_2 - V_1)}$$

Here v (V s^{-1}) is the scan rate, (V_2-V_1) is the potential window, A (cm^2) is the area of working electrode. The values of areal capacitance of the developed samples at different scan rates (2 mV s^{-1}–100 mV s^{-1}) are given in Table 2.

The successive increase in current values of porous samples as compared to sample S1, indicated the increase of ionic conductivity with increase in porosity. High surface area and directed channels in porous samples resulted in more intense peaks and higher capacitance values than S1 [38]. The decrease in capacitance values of all samples with the increase in scan rates was attributed to the diffusion limitations of the charge carriers and electrolyte ions into the inside of electrode at higher scan rates [47,48]. The current response of all the samples was found to increase with the increase in scan rate, which points toward the excellent kinetics and reversibility of the electrode [29]. The presence of redox peaks even at 100 mV s^{-1} (Fig. 9), indicated that the developed materials have good rate capability.

3.2.2. *Galvanostatic charge-discharge analysis*

The galvanostatic charge-discharge (GCD) analysis of as-cast S1 and FS2-FS5 samples was performed to assess the charge discharge behavior and rate capability of the samples. GCD analysis of the studied samples was carried out over the same potential window (−1 V–+1 V) with same three electrode electrochemical setup as used in CV measurements, at current densities of 100, 300, 500, and 700 μA cm^{-2}. The relatively

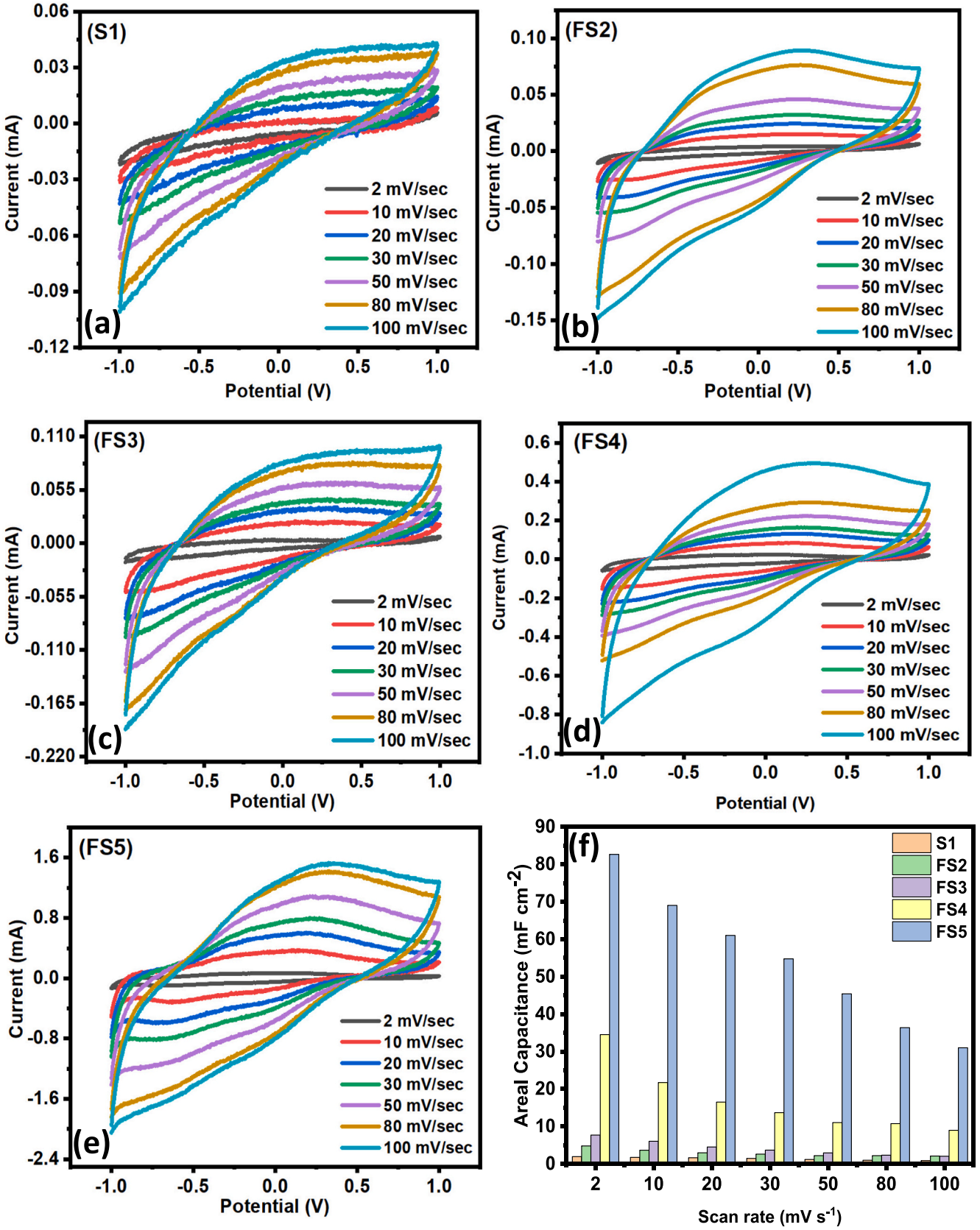

Fig. 10. Cyclic voltammograms of (a) as-cast S1 (b) FS2 (c) FS3 (d) FS4 (e) FS5 and (f) comparison of the capacitance values of samples as a function of scan rates.

Table 2
Areal capacitance (Ca) values of all the samples calculated from CV data.

Scan rate (mV s^{-1})	Capacitance (mF cm^{-2})				
	S1	FS2	FS3	FS4	FS5
2	1.96	4.82	7.70	34.54	82.66
10	1.76	3.66	6.06	21.73	69.06
20	1.65	2.97	4.52	16.53	61.04
30	1.47	2.61	3.70	13.70	54.78
50	1.20	2.22	2.94	11.05	45.44
80	0.98	2.22	2.33	10.76	36.40
100	0.90	2.12	2.05	8.99	31.03

symmetrical potential–time curves can be observed (Fig. 11). Each curve has displayed distinct potential plateaus and the deviation of GCD curves from linearity reveals that the charge storage mechanism is due to both faradic pseudocapacitive reaction [49] and charge adsorption on sample surface and is also consistent with the redox peaks in CV curves [50]. Like CV results, the FS5 sample showed the best performance in the GCD analysis, which implies that the electrode performance is highly reproduceable and consistent.

3.2.3. Electrochemical impedance spectroscopy analysis

Electrochemical impedance spectroscopy (EIS) measurements were performed at 10 mV amplitude in frequency range of 100 kHz–10 MHz to understand the kinetic properties. The Nyquist plot of all the samples from low to high frequency regions is shown in Fig. 11(f). The high frequency intercept on the real axis (Z′) represented the series resistance (RΩ), which corresponded to the combination of electrolyte (ionic) resistance, internal resistance of active material, and the contact resistance at the electrode/electrolyte interface [51]. The EIS data was fitted with equivalent circuit according to the shape of Nyquist plot (shown as an inset of Fig. 11f) [52,53]. Samples S1, FS2, FS3, FS4, and FS5 showed the Rs (series resistance) values of 11.01 Ω, 7.03 Ω, 6.41 Ω, 4.37 Ω and 2.19 Ω respectively. The Rs values indicated that the internal resistance of electrode material and the contact resistance at the electrode/electrolyte interface decreased with the increase in porosity (FS2–FS5) which boosted the ionic conductivity, and hence improved the rate capability for superior supercapacitor applications.

The fitted EIS data is also consistent with the CV and GCD testing, where FS5 sample showed higher areal capacitances against other samples, indicating stable and highly reproduceable electrochemical

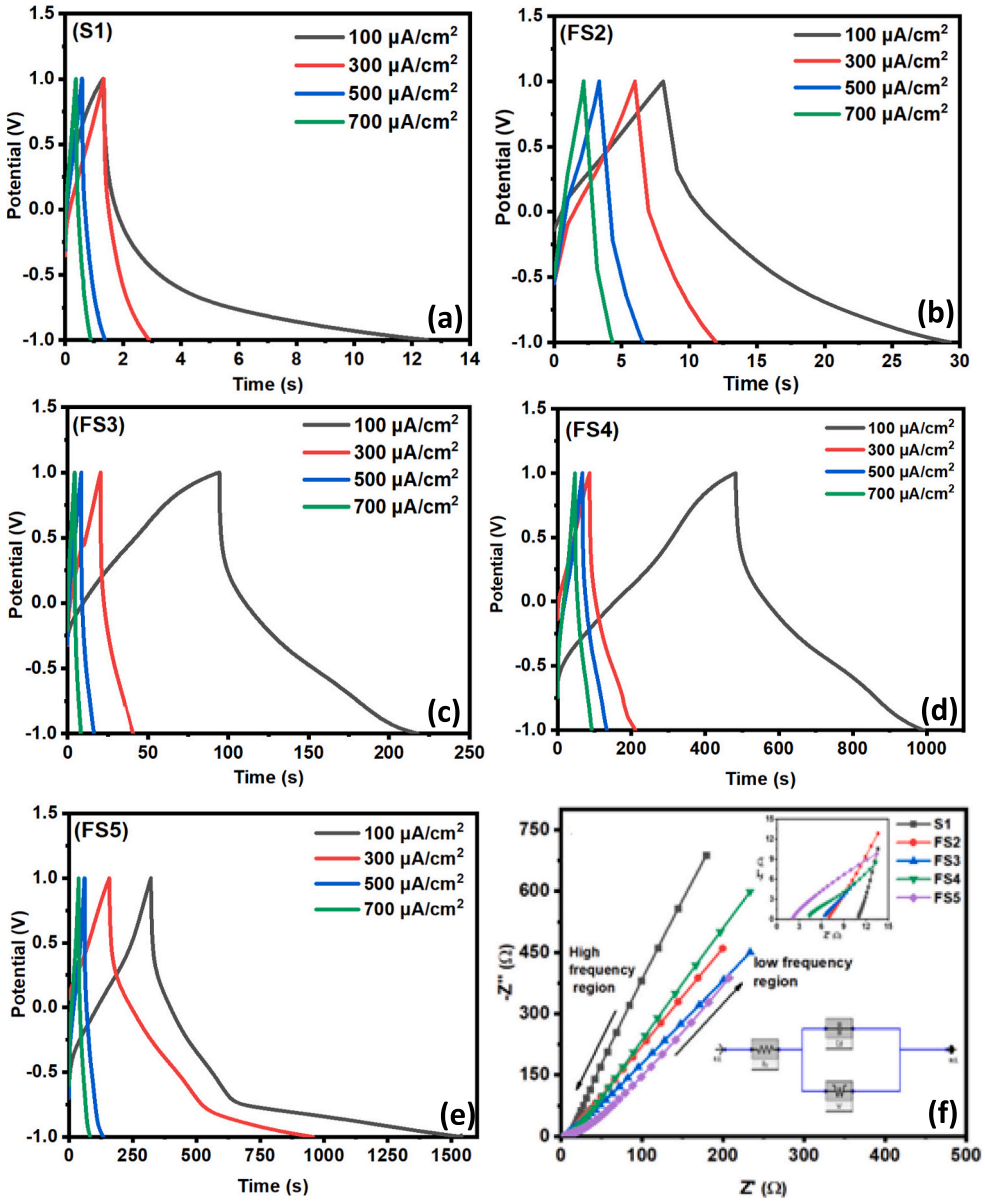

Fig. 11. Galvanostatic charge-discharge curves of (a) as-cast S1 (b) FS2 (c) FS3 (d) FS4 (e) FS5 and (f) Nyquist plots of S1-FS5 samples.

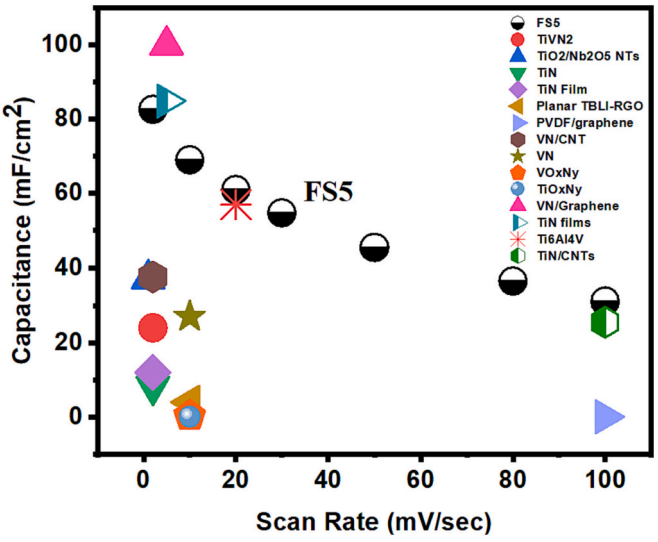

Fig. 12. Comparison of areal capacitance of FS5 with the data from literature [54–65].

characteristics of the sample. The reason for this superior electrochemical property of the FS5 sample against others was attributed to its high porosity which provided higher active sites and hence higher utilization of active material. The capacitance value obtained for sample FS5 is considerably higher than the previously reported values of refractory metal oxides, nitrides and other carbon-based materials. Comparison of capacitance values obtained from present study with literature are shown in Fig. 12 and Table 3.

As shown in Table 3 and Fig. 12, the value of aerial capacitance obtained for FS5 (82.66 mF cm^{-2} at 2 mV s^{-1}) is considerably higher than the values reported for different binary refractory metal oxides and nitrides.

Long cycling life with strong capacity retention is an important requirement for enhanced electrochemical performance of supercapacitor in practical applications. The capacity retention graph of FS5 sample for 5000 cycles at a current density of 1 mA cm^{-2} is shown in the Fig. 13 (a). FS5 was found to retain 104 % of its initial capacitance value after 5000 cycles, indicating its strong stability and rate capability of electrode which was attributed to the good structural stability of HEA that prevented the expansion and contraction of electrodes [6]. The electrode displayed coulombic efficiency of 96.35 %. Ragone plots for FS2-FS5 electrodes are presented in Fig. 13 (b), which represents the energy and power performances of these electrodes. Ragone plots are generally used for packaged device but with the advent of new electrode materials with novel morphologies it would be appropriate to isolate the energy/power performance of individual components of the half-cell (like electrolyte or electrode) to understand the effect of these components on the overall electrochemical performance [66]. Energy density ($E.d = \frac{1}{2}CV^2$) and power density ($P.d = (E.d)/\Delta t$) were calculated by using the GCD curves. FS5 has shown a better combination of energy density and power density compared to other electrodes which is consistent with the CV and GCD results. Developed high entropy foams in general and FS5 in particular showed superior electrochemical properties in comparison to the ones reported previously for transition metal oxides. It is believed that insertion of interconnected porosity by

Table 3
Comparison of areal capacitance of current study with various materials reported in literature.

#	Material	Electrolyte	Scan rate (mV s^{-1})	Capacitance (mF cm^{-2})	Refs
1	Planar TBLI-RGO porous films	PVA–H_3PO_4	10	3.97	[54]
2	PVDF/graphene films	1 M H_3PO_4	100	0.0059	[55]
3	VN thin films	1 M KOH	10	27	[56]
4	VOxNy powder	1 M KOH	10	0.3	[67]
	TiOxNy powder	1 M KOH	10	0.05	
5	TiO_2/Nb_2O_5 NTs	1 M H_2SO_4	1	37	[58]
6	Mn-decorated Zr-MOF-CNT nanocomposites	0.1 M Na_2SO_4	50	4.9	[59]
7	Ti_6Al_4V electrode	1.0 M Li_2SO_4	20	57	[60]
8	TiN porous films	1 M KCl	2	84.9	[61]
9	TiN film	0.5 M K_2SO_4	2	12	[62]
10	**NbTiVZrY**	**1 M Na_2SO_4**	**2**	**82.66**	**This work**

Bold values in the table specify/highlight the findings of the current study when compared to those found in literature.

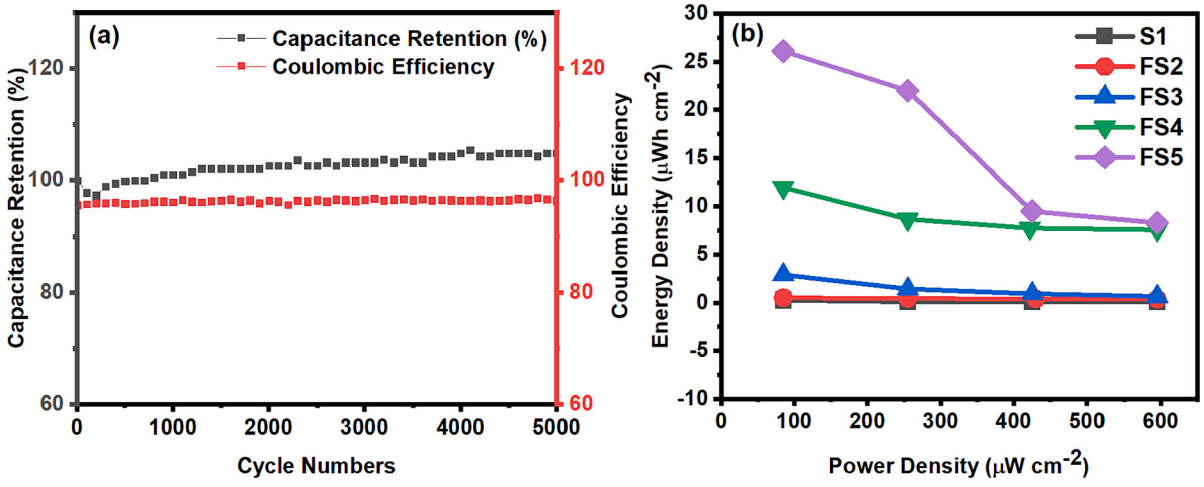

Fig. 13. (a) Cyclic stability of FS5 sample at current density of 1 mA cm^{-2} (b) Plots of power density versus energy density of all samples.

the adopted has shortened the electrons transmission path and provided higher active surface sites for better utilization of the active material [29] thereby allowing faster and more efficient charge/discharge ability. The developed HEA electrodes have demonstrated better electrochemical performance than metal oxides, nitrides and thin film-based electrodes primarily due to the synergistic effect of the components of HEA system and more electroactive sites available for charge storage.

4. Conclusion

NiTiVZr foams have been successfully developed by the insertion of yttrium in the base HEA and its removal by electrochemical dealloying process. Developed foams displayed excellent electrochemical properties. FS5 exhibited the highest areal capacitance value of 85mF cm^{-2} at the scan rate of 2 mV s^{-1}. FS5 electrode also demonstrated high cyclic stability and displayed capacitance retention of 104 % after 5000 cycles at 1 mA cm^{-2} current density. The outstanding electrochemical properties of developed foams was attributed to the presence of higher surface adsorption sites in the samples and porous network which facilitated higher ion diffusion and improved electrochemical interactions resulting in lower ESR values.

Declaration of competing interest

The authors declare that they have no known competing financial interests or personal relationships that could have appeared to influence the work reported in this paper.

Data availability

Data will be made available on request.

Acknowledgement

Financial support from Higher Education Commission of Pakistan (HEC NRPU 6019) is acknowledged.

References

[1] K.K. Upadhyay, et al., Capacitance response in an aqueous electrolyte of Nb2O5 nanochannel layers anodically grown in pure molten o-H3PO4 281 (2018) 725–737.
[2] Z. Yu, et al., Supercapacitor electrode materials: nanostructures from 0 to 3 dimensions 8 (3) (2015) 702–730.
[3] M. Naeem Ashiq, et al., Enhanced electrochemical properties of silver-coated zirconia nanoparticles for supercapacitor application 15 (1) (2021) 10–16.
[4] K. Kong, et al., Nanoporous structure synthesized by selective phase dissolution of AlCoCrFeNi high entropy alloy and its electrochemical properties as supercapacitor electrode 437 (2019) 226927.
[5] Z.S. Iro, C. Subramani, S.S. Dash, A brief review on electrode materials for supercapacitor 11 (12) (2016) 10628–10643.
[6] H. Zhou, J. He, Synthesis of the New High Entropy Alloy and Its Application in Energy Conversion and Storage 8, 2020, p. 73.
[7] T. Zhao, et al., In situ synthesis of interlinked three-dimensional graphene foam/polyaniline nanorod supercapacitor 230 (2017) 342–349.
[8] M. Inagaki, H. Konno, O. Tanaike, Carbon materials for electrochemical capacitors 195 (24) (2010) 7880–7903.
[9] M.R.A. Karim, M. Noman, K.I. Khan, W. Shehzad, E.U. Haq, N. Shahzad, K. Yaqoob, Solvothermal synthesis of flower-flakes like nano composites of Ni-co metal organic frameworks and graphene nanoplatelets for energy storage applications, ECS J. Solid State Sci. Technol. 11 (1) (2022), 011001.
[10] S.S. Haider, M.Z. Iqbal, S. Zakar, A.M. Afzal, K. Yaqoob, S. Aftab, Superior performance of electrodeposited CoMnS as novel electrode material for supercapattery devices, J. Energy Storage 39 (2021) 102608.
[11] M.Z. Iqbal, S. Alam, A.M. Afzal, M.J. Iqbal, K. Yaqoob, M.A. Kamran, T. Alherbi, Binary composites of strontium oxide/polyaniline for high performance supercapattery devices, Solid State Ion. 347 (2020) 115276.
[12] W. Khalid, M.R. Abdul Karim, M. Atif, W. Shehzad, M.A. Marwat, K. Yaqoob, Ultrasounds-assisted solvothermal synthesis of Ni-Co-Mn MOFs/PANI-CNTs nanocomposites with enhanced electrochemical energy storage performance, Energy Environ. (2023), https://doi.org/10.1177/0958305X231196126.
[13] I. Shown, et al., Conducting polymer-based flexible supercapacitor 3 (1) (2015) 2–26.
[14] R. Basu, et al., Phase-pure VO2 nanoporous structure for binder-free supercapacitor performances 9 (1) (2019) 1–11.
[15] R.S. Ganji, P.S. Karthik, K.B.S. Rao, K.V. Rajulapati, Strengthening mechanisms in equiatomic ultrafine grained AlCoCrCuFeNi high-entropy alloy studied by micro- and nanoindentation methods, Acta Mater. 125 (2017) 58–68.
[16] S. Singh, N. Wanderka, B.S. Murty, U. Glatzel, J. Banhart, Decomposition in multi-component AlCoCrCuFeNi high-entropy alloy, Acta Mater. 59 (1) (2011) 182–190.
[17] M. Vaidya, K. Guruvidyathri, B.S. Murty, Phase formation and thermal stability of CoCrFeNi and CoCrFeMnNi equiatomic high entropy alloys, J. Alloys Compd. 774 (2019) 856–864.
[18] Z. Jin, J. Lv, H. Jia, W. Liu, H. Li, Z. Chen, H.J. Qiu, Nanoporous Al-Ni-Co-Ir-Mo high-entropy alloy for record-high water splitting activity in acidic environments, Small 15 (47) (2019) 1904180.
[19] K. Kong, J. Hyun, Y. Kim, W. Kim, D. Kim, Nanoporous structure synthesized by selective phase dissolution of AlCoCrFeNi high entropy alloy and its electrochemical properties as supercapacitor electrode, J. Power Sources 437 (2019) 226927.
[20] H.J. Qiu, G. Fang, J. Gao, Y. Wen, J. Lv, H. Li, S. Sun, Noble metal-free nanoporous high-entropy alloys as highly efficient electrocatalysts for oxygen evolution reaction, ACS Mater. Lett. 1 (5) (2019) 526–533.
[21] K. Li, Y. Zhai, M. Lai, M. Song, S. Zou, G. Huang, N. Zhang, Corrosion of eutectic high-entropy alloys: a review, Crystals 13 (8) (2023) 1231.
[22] M. Abdullah, M. Mukarram, T.B. Yaqub, F. Fernandes, K. Yaqoob, Development of eutectic high entropy alloy by addition of W to CoCrFeNi HEA, Int. J. Refractory Metals Hard Mater. (2023) 106300.
[23] M.A. Mehmood, M. Mujahid, A. Godfrey, M.F. Zafar, K. Yaqoob, Development and characterization of boride-reinforced CoCrFeNi composites, J. Alloys Compd. 947 (2023) 169535.
[24] M.A. Mehmood, K. Shehzad, M. Mujahid, T.B. Yaqub, A. Godfrey, F. Fernandes, K. Yaqoob, Ceramic-reinforced HEA matrix composites exhibiting an excellent combination of mechanical properties, Sci. Rep. 12 (1) (2022) 21486.
[25] S.W. Hussain, M.A. Mehmood, M.R.A. Karim, A. Godfrey, K. Yaqoob, Microstructural evolution and mechanical characterization of a WC-reinforced CoCrFeNi HEA matrix composite, Sci. Rep. 12 (1) (2022) 9822.
[26] M. Mukarram, M.A. Munir, M. Mujahid, K. Yaqoob, Systematic development of eutectic high entropy alloys by thermodynamic modeling and experimentation: an example of the CoCrFeNi-Mo system, Metals 11 (9) (2021) 1484.
[27] M. Mukarram, M. Mujahid, K. Yaqoob, Design and development of CoCrFeNiTa eutectic high entropy alloys, J. Mater. Res. Technol. 10 (2021) 1243–1249.
[28] P.-C. Chen, et al., Selectively dealloyed Ti/TiO2 network nanostructures for supercapacitor application 133 (2014) 175–178.
[29] A.N. Banerjee, V. Anitha, S.W.J.S.r. Joo, Improved electrochemical properties of morphology-controlled titania/titanate nanostructures prepared by in-situ hydrothermal surface modification of self-source Ti substrate for high-performance supercapacitors 7 (1) (2017) 1–20.
[30] S.K. Das, S. Darmakolla, A.J. Bhattacharyya, High lithium storage in micrometre sized mesoporous spherical self-assembly of anatase titania nanospheres and carbon 20 (8) (2010) 1600–1606.
[31] S. Yoon, et al., Development of a high-performance anode for lithium ion batteries using novel ordered mesoporous tungsten oxide materials with high electrical conductivity 13 (23) (2011) 11060–11066.
[32] J.K. Shon, et al., Nano-propping effect of residual silicas on reversible lithium storage over highly ordered mesoporous SnO 2 materials 19 (37) (2009) 6727–6732.
[33] J. Cho, Porous Si anode materials for lithium rechargeable batteries 20 (20) (2010) 4009–4014.
[34] F.-S. Ke, et al., Fabrication and properties of macroporous tin–cobalt alloy film electrodes for lithium-ion batteries 170 (2) (2007) 450–455.
[35] M. Mancini, et al., Mesoporous anatase TiO2 composite electrodes: electrochemical characterization and high rate performances 189 (1) (2009) 585–589.
[36] A. Vu, Y. Qian, A.J.A.E.M. Stein, Porous electrode materials for lithium-ion batteries–how to prepare them and what makes them special 2 (9) (2012) 1056–1085.
[37] H. Huang, et al., Facile one-step forming of NiO and yttrium-stabilized zirconia composite anodes with straight open pores for planar solid oxide fuel cell using phase-inversion tape casting method 274 (2015) 1114–1117.
[38] L. Hu, et al., Control of pore channel size during freeze casting of porous YSZ ceramics with unidirectionally aligned channels using different freezing temperatures 30 (16) (2010) 3389–3396.
[39] D.-X. Qiao, et al., A novel series of refractory high-entropy alloys Ti2ZrHf0. 5VNbx with high specific yield strength and good ductility 32 (8) (2019) 925–931.
[40] K. Yaqoob, K.N. Yoon, E.S. Park, Body-centered Cubic High-entropy Alloy Foam and Manufacturing Method for the Foam, Republic of Korea, KR No. 10-1773298, Aug 24, 2017 (Registered).
[41] P. De, et al., Role of Porosity and Diffusion Coefficient in Porous Electrode Used in Supercapacitors–Correlating Theoretical and Experimental Studies, 2022, p. e2100159.
[42] P.J.E.A. Haldar, Achieving wide potential window and high capacitance for supercapacitors using different metal oxides (viz.: ZrO2, WO3 and V2O5) and their PANI/graphene composites with Na2SO4 electrolyte 381 (2021) 138221.
[43] C. Zhong, et al., A review of electrolyte materials and compositions for electrochemical supercapacitors 44 (21) (2015) 7484–7539.
[44] P. Haldar, et al., Mn3O4-polyaniline-graphene as distinctive composite for use in high-performance supercapacitors 491 (2019) 171–179.
[45] K. Fic, et al., Novel insight into neutral medium as electrolyte for high-voltage supercapacitors 5 (2) (2012) 5842–5850.

[46] M. Zhen, et al., TiO 2–B nanorods on reduced graphene oxide as anode materials for Li ion batteries 51 (3) (2015) 507–510.
[47] M. Salari, et al., Enhancement of the electrochemical capacitance of TiO 2 nanotube arrays through controlled phase transformation of anatase to rutile 14 (14) (2012) 4770–4779.
[48] Q. Ke, et al., 3D TiO2@ Ni (OH) 2 core-shell arrays with tunable nanostructure for hybrid supercapacitor application 5 (1) (2015) 1–11.
[49] S. Li, et al., In situ XPS studies of thermally deposited potassium on poly (p-phenylene vinylene) and its ring-substituted derivatives 181 (3–4) (2001) 201–210.
[50] Y. Zhang, Y. Huang, Facile synthesis and characterization of rough surface V 2 O 5 nanomaterials for pseudo-supercapacitor electrode material with high capacitance 40 (6) (2017) 1137–1149.
[51] C. Wan, L. Yuan, H. Shen, Effects of electrode mass-loading on the electrochemical properties of porous MnO2 for electrochemical supercapacitor 9 (7) (2014) 4024–4038.
[52] W. Zhao, et al., Enhanced photocatalytic activity for H2 evolution under irradiation of UV–Vis light by Au-modified nitrogen-doped TiO2 9 (8) (2014) e103671.
[53] H. Wang, et al., General and controllable synthesis strategy of metal oxide/TiO2 hierarchical heterostructures with improved lithium-ion battery performance 2 (1) (2012) 1–8.
[54] X.-Y. Fu, et al., Free-standing and flexible graphene supercapacitors of high areal capacitance fabricated by laser holography reduction of graphene oxide 118 (7) (2021) 071601.
[55] V.T. Le, et al., Simultaneous enhancement of specific capacitance and potential window of graphene-based electric double-layer capacitors using ferroelectric polymers 507 (2021) 230268.
[56] G. Durai, et al., Influence of chromium content on microstructural and electrochemical supercapacitive properties of vanadium nitride thin films developed by reactive magnetron co-sputtering process 45 (10) (2019) 12643–12653.
[57] R.L. Porto, et al., Titanium and vanadium oxynitride powders as pseudo-capacitive materials for electrochemical capacitors 82 (2012) 257–262.
[58] S. Ozkan, et al., Highly Conducting Spaced TiO $ _2 $ Nanotubes Enable Defined Conformal Coating with Nanocrystalline Nb $ _2 $ O $ _5 $ and High Performance Supercapacitor Applications, 2020.
[59] Y.S. Wang, et al., Toward metal–organic-framework-based supercapacitors: room-temperature synthesis of electrically conducting MOF-based nanocomposites decorated with redox-active manganese 2019 (26) (2019) 3036–3044.
[60] C. Zhao, et al., Three dimensional (3D) printed electrodes for interdigitated supercapacitors 41 (2014) 20–23.
[61] N. Sun, et al., Sputtered titanium nitride films with finely tailored surface activity and porosity for high performance on-chip micro-supercapacitors 489 (2021) 229406.
[62] A. Achour, et al., Titanium nitride films for micro-supercapacitors: effect of surface chemistry and film morphology on the capacitance 300 (2015) 525–532.
[63] A. Achour, et al., Role of nitrogen doping at the surface of titanium nitride thin films towards capacitive charge storage enhancement 359 (2017) 349–354.
[64] A. Achour, et al., Hierarchical nanocomposite electrodes based on titanium nitride and carbon nanotubes for micro-supercapacitors 7 (2014) 104–113.
[65] A. Ramadoss, et al., Construction of light-weight and flexible vanadium nitride coated graphite paper electrodes for supercapacitors 28 (5) (2022) 2513–2524.
[66] L. Mai, et al., Fast ionic diffusion-enabled nanoflake electrode by spontaneous electrochemical pre-intercalation for high-performance supercapacitor 3 (1) (2013) 1–8.